MODELING THE EVOLUTION OF FATIGUE FAILURE WITH PERIDYNAMICS

GUANFENG ZHANG, FLORIN BOBARU

Abstract. Holes and round notches are locations where fatigue cracks may arrest. Investigating the evolution of fatigue cracks after sinking into such a hole is important. Here we extend a recently proposed fatigue crack peridynamic model to treat such cases. The proposed improvements add the fatigue limit to the propagation phase. We demonstrate that the model simulates the three phases of fatigue failure (initiation, propagation, and final failure) with an example in which a fatigue crack sinks into a cutout and re-initiates from a different location along the cutout, grows, and lead to final failure of the structure. The fatigue crack path from the improved model agrees with an analysis based on strain concentrations. Convergence studies show that the peridynamic results are correct once the nonlocal size is smaller compared with the size of relevant geometrical features. We also discuss acceleration of computations on GPU-enabled hardware, obtained with minimal changes to a serial code.

Key words: fatigue crack, peridynamics, crack propagation, crack initiation, fatigue life, fracture.

1. INTRODUCTION

Fatigue cracking is a main failure mode for many engineering materials and structures. Extensive efforts have been dedicated to simulate fatigue crack paths and fatigue life [1]. Most of these modeling works are based on classical mechanics, like the Finite Element Method (FEM) or the Extended FEM (XFEM). These types of methods, when applied to modeling of material failure and damage, require various criteria to determine the crack growth direction, like the maximum circumferential stress, the maximum energy release rate, or the minimum strain energy density [2], the crack extension etc. Usually cracks either are constrained to follow the element sides, or else the crack path has to be "tracked" and explicitly represented, via, for example, level sets [3, 4].

In the continuum theory, named peridynamics, proposed in [5], damage and fracture are an integral part of the formulation. This theory is based on integral equations, and spatial derivatives of the unknown displacement field are not present, making it

University of Nebraska-Lincoln, Lincoln, NE 68588-0526

Ro. J. Techn. Sci. – Appl. Mechanics, Vol. 61, N° 1, pp. 22–40 , Bucharest, 2016

easy to deal with problems in which discontinuities appear in the solution, as in the case of fatigue fracture, for example. The peridynamic model has been successfully used to predict the crack growth velocity and crack patterns in dynamic brittle fracture [6, 7], damage and fracture in composite laminates [8–10], functionally graded materials [11] etc. Most of these works were dedicated to simulating damage and fracture under dynamic loading. A peridynamic fatigue cracking model was recently proposed by Silling and Askari [12] to simulate crack growth under cyclic loading. This was the first time that a single model could simulate the three phases of fatigue cracking: crack nucleation, crack propagation, and final failure. This peridynamic fatigue model has the following characteristics: 1) allows growth of multiple cracks and complex crack interactions; 2) cracks and damage grow autonomously; 3) tracking of the crack path is not necessary. The details of the numerical implementation of this fatigue cracking model are provided in [13]. In reference [13], a set of damage factors were introduced to improve the computational efficiency while maintaining numerical stability of the model.

As a non-local method, peridynamic simulations are computationally more expensive than local methods. To improve computational efficiency, an acceleration method is proposed here, speeding up the internal force calculations, which are the most computationally intensive part of a peridynamic static or dynamic solver. By taking advantage of the CUDA-enabled GPU devices, the proposed GPU algorithm is significantly faster than serial CPU code. Memory usage analysis shows that the proposed acceleration method allows simulations of problems with a large number of unknowns.

In the original peridynamic fatigue model, the crack propagation phase is calibrated to Paris' law data. However, this model ignored the fact that the Paris' law is not valid when the stress intensity range is smaller than its threshold. We observe that ignoring the threshold, the remaining life of bonds continues to decrease around developed crack paths, independent on whether the threshold is met or not. We explain this issue by simulating a modified compact tension test. Results indicate that the original model leads to the fatigue crack sinking into the hole, as expected, but when simulations are continued, instead of a new crack being initiated somewhere on the other side of the hole, damage forms around the original crack and an unphysical fatigue crack path is obtained instead. We extend the model to incorporate a "fatigue limit", calculated based on the threshold stress intensity range, in the crack propagation phase. We provide convergence results for crack paths and fatigue lives, under reducing the size of the nonlocal region (and refining, correspondingly, the grid spacing), for a relatively complex fatigue crack growth scenario. Crack paths agree with the strain concentrations produced by quasi-static elastic analysis. The peridynamic model for fatigue fracture is able to continue the simulations through full failure of the sample, and we observe the expected large rotations of the sample past final failure. The results demonstrate the effectiveness of the proposed extension in modeling of complex fatigue crack growth.

2. PERIDYNAMIC FORMULATION

In peridynamics, each material point **x** in a solid body is connected to its neighbors within a "horizon" region $H_{\mathbf{x}}$ (usually taken as a sphere in 3D or disk in 2D of radius δ) through peridynamic bonds. The peridynamic formulation for the equations of motion is given as [5]:

$$\rho\,\ddot{\mathbf{u}}(\mathbf{x},t)=\int_{H_{\mathbf{x}}}\mathbf{f}(\boldsymbol{\eta},\boldsymbol{\xi})\,\mathrm{d}\mathbf{V}_{\mathbf{x}'}+\mathbf{b}(\mathbf{x},t)\,, \tag{1}$$

where ρ is the density, **u** is the displacement vector, **f** is the pairwise force in a peridynamic bond which connects point **x′** and **x**, and $\mathbf{V}_{\mathbf{x}'}$ is the volume/area of point **x′** covered by the horizon of point **x**, and **b** is the external force density. We denote by $\boldsymbol{\xi}$ the relative position $\boldsymbol{\xi}=\mathbf{x}'-\mathbf{x}$ in the reference configuration and by $\boldsymbol{\eta}$ the relative displacement $\mathbf{u}(\mathbf{x}',t)-\mathbf{u}(\mathbf{x},t)$.

For elastic materials, the pairwise force in the equation above is determined by the peridynamic potential ω

$$\mathbf{f}(\boldsymbol{\eta},\boldsymbol{\xi})=\frac{\partial\omega(\boldsymbol{\eta},\boldsymbol{\xi})}{\partial\boldsymbol{\eta}}, \tag{2}$$

where ω is the micro-potential. For a *linear microelastic material* [14], the micro-potential is

$$\omega(\boldsymbol{\eta},\boldsymbol{\xi})=\frac{c(\xi)s^2\|\boldsymbol{\xi}\|}{2}, \tag{3}$$

where $c(\xi)$ is the micromodulus function and s is bond strain, $s=\left(|\boldsymbol{\eta}+\boldsymbol{\xi}|-|\boldsymbol{\xi}|\right)\big/|\boldsymbol{\xi}|$. In peridynamics, a bond can break irreversibly when bond strain $s\geq s_0$, where s_0 is the critical value of bond strain. The parameter that defines the micromodulus function are calibrated with the elastic material properties by matching the classical elastic strain energy density to the peridynamic strain energy density for a homogeneous deformation. Similar to the derivation for the plane stress conditions in [13], we can find the micromodulus function for the plane strain conditions, which will be used in the following sections because the experimental fatigue tests are performed on thick samples. Thus, for a 2D model with plane strain assumption, and assuming a "conical" shape for the micro-modulus as a function of the bond length, we have:

$$c(\boldsymbol{\xi})=\frac{24E}{(1-\nu-2\nu^2)\pi\delta^3}\left(1-\frac{|\boldsymbol{\xi}|}{\delta}\right), \tag{4}$$

in which E is Young's modulus and ν is the Poisson ratio (fixed to ¼ in 2D plane strain for bond-based peridynamics). To improve the numerical accuracy, we use the conical micromodulus, see detailed discussion in [15]. The critical bond strain

is calibrated to the material's fracture energy and, for the selected micromodulus, found to be given by:

$$s_0 = \sqrt{\frac{25\pi G_0}{48E\delta}}, \tag{5}$$

where G_0 is the critical energy release rate for mode I fracture, measured from experiments.

The damage index is defined in peridynamics to monitor the evolution of damage at every material point in the body. Usually, cracks do not have to be tracked in peridynamics, instead, in a damage index plot cracks show up as localized regions with points on either side of the crack surface having a damage index of about 0.5.

Using the meshfree-type grid introduced in [14], the damage at a node is defined by: $d = n^{\text{broken}}/n$, where n^{broken} and n are the number of broken peridynamic bonds connected with the node and the original number of bonds for this node, respectively. The damage index ranges between 0 and 1, with "0" meaning no bonds are broken, and "1" meaning all bonds are broken.

3. PERIDYNAMIC MODEL FOR FATIGUE CRACKING

In the peridynamic fatigue cracking model, each bond has a parameter named remaining life λ [12]. The value of λ is 1 for an intact bond and it is monotonically decreasing as the cycle number N increases. A bond breaks due to fatigue once $\lambda(N) \le 0$. The remaining life evolves according to

$$\frac{\mathrm{d}\lambda(N)}{\mathrm{d}N} = -A\varepsilon^p, \tag{6}$$

where $\varepsilon = \left| s^{\max} - s^{\min} \right|$ is the current strain range in this bond, $s^{\max}$ and $s^{\min}$ are the maximum and minimum bond strains in this cycle. A and p are two positive constants to be calibrated separately: A_1 and p_1 from phase I (fatigue crack nucleation phase) and A_2 and p_2 from phase II (fatigue crack propagation phase).

In phase I, two parameters are calibrated with S-N curve data. By integrating eq. (6) from the zero-th cycle to the cycle N_1 at which the first bond breaks, we get:

$$N_1 = \frac{1}{A_1 \varepsilon^{p_1}}. \tag{7}$$

Enforcing the match between eq. (7) with an experimental S-N curve in terms of strains, values of A_1 and p_1 can be obtained [12].

In phase II, the value of the remaining life of a bond $\lambda_{i,j}^n$, which connects nodes $\mathbf{x}_i$ and $\mathbf{x}_j$, evolves according to eq. (6). The discretized form of this equation is

$$\lambda_{i,j}^{0}=1,\quad \frac{\lambda_{i,j}^{n}-\lambda_{i,j}^{n-1}}{\Delta t}=-A_2\left(\varepsilon_{i,j}^{n}\right)^{p_2}, \tag{8}$$

in which $\varepsilon_{i,j}^{n}$ is the cyclic strain range at step n, Δt is the "time" step length for the fictitious time t, which is a linear map to cycle number N: $N=t/\tau$, where τ is a positive constant. Values A_2 and p_2 can be calibrated by comparing the crack growth rate in the peridynamic fatigue model

$$\frac{\mathrm{d}a}{\mathrm{d}N}=\beta A_2\,\varepsilon^{p_2}, \tag{9}$$

with Paris's law

$$\frac{\mathrm{d}a}{\mathrm{d}N}=c\Delta K^{M}. \tag{10}$$

Here, β represents the geometry influence on the strain distribution, c and M are constants determined from experiments, and ΔK is the stress intensity range. More detailed explanations can be found in [13].

4. AN EXTENSION OF THE PERIDYNAMIC FATIGUE MODEL

The fatigue limit is the amplitude of cyclic stress below which the material can be cycled for either an infinite or a sufficient number of cycles without fracture [16]. In [12], the fatigue limit is incorporated in the crack initiation phase by modifying the evolution law of remaining life (Eq. (6)) as follows:

$$\frac{\mathrm{d}\lambda(N)}{\mathrm{d}N}=\begin{cases}-A_1(\varepsilon-\varepsilon_\infty)^{p_1}, & \text{if } \varepsilon>\varepsilon_\infty,\\ 0 & \text{otherwise.}\end{cases} \tag{11}$$

In this equation, ε_∞ is the fatigue limit expressed in terms of strains, for the crack initiation phase. Numerical examples in the remaining sections show the implementation details of phase I model with this fatigue limit.

As discussed above, the phase II of this peridynamic fatigue model is calibrated by matching with experimental Paris' law, which relates the range of stress intensity factor and the crack propagation rate. Because the crack ceases to advance if the stress intensity range is smaller than a threshold value ΔK_{th} [17], we introduce an extension of the model to incorporate the threshold stress-intensity range. Similar to Eq. (11), we can modify the crack propagation law in Eq. (6) by adding a fatigue limit $\tilde{\varepsilon}_\infty$ for the crack propagation phase, as follows:

$$\frac{\mathrm{d}\lambda(N)}{\mathrm{d}N} = \begin{cases} -A_2 \varepsilon^{p_2}, & \text{if } \varepsilon > \tilde{\varepsilon}_\infty, \\ 0 & \text{otherwise.} \end{cases} \tag{12}$$

Because the range of stress intensity is proportional to the strain, $\tilde{\varepsilon}_\infty$ can be calculated based on the following equation:

$$\frac{\tilde{\varepsilon}_\infty}{\overline{\varepsilon}} = \frac{\Delta K_{\mathrm{th}}}{\Delta K}, \tag{13}$$

in which $\overline{\varepsilon}$ is the average cyclic strain of bonds connected to the crack tip. In this way, the remaining life λ is "frozen" if $\Delta K < \Delta K_{\mathrm{th}}$. This prevents unphysical fatigue crack propagation. To accomplish this step, here we do need to track the crack tip. For a general algorithm that tracks the crack tips of any number of cracks, based on Matlab's image processing functions, please see [13]. Once the crack tip location is determined, we compute the peridynamic J-integral on a contour surrounding it, as discussed in [13]. This works until a crack sinks into an existing perforation, hole, or defect, when the contour may need to be modified so that it surrounds such holes or defects as well. We then compute the stress-intensity range and compare with the threshold value to decide whether we modify the remaining life or not.

5. NUMERICAL IMPLEMENTATION AND GPU ACCELERATION

A peridynamic fatigue simulation uses repeated calls to a peridynamic quasi-static solver. The quasi-static solution, at every fictitious fatigue time step, updates the remaining life of bonds in phase I and phase II until a bond breaks because its remaining life reaches zero. A bond can also break, in phase III, if it reaches the critical bond strain criterion [14]. Details of the numerical implementation, including the peridynamic J-integral for calculating the stress intensity factor, are provided in [13]. In reference [13] we also introduced a set of damage index factors that improve stability and efficiency of computations in the peridynamic fatigue fracture model.

In this section, we briefly review the numerical implementation and discuss a GPU-based implementation and its advantages.

A nonlinear system of equations, with nodal displacements as unknowns, result from discretizing the quasi-static peridynamic equations:

$$\int_{\mathrm{H_x}} \mathbf{f}(\boldsymbol{\eta}, \boldsymbol{\xi}, t)\, \mathrm{d}\mathbf{V}_{\mathbf{x}'} + \mathbf{b}(\mathbf{x}, t) = 0, \tag{14}$$

where t is the fictitious fatigue time introduced before. The numerical quadrature used here is the partial volume integration algorithm given in [6, 20]. We solve the system by using the nonlinear (Polak-Ribière) conjugate gradient (CG) method [18]. A comprehensive discussion of CG implementation, including calculating the CG direction and general line search methods are in [19]. We start the CG solver with the steepest direction and use the secant method to search for the next point along the CG step. The stopping criterion used for the CG iterations in the computations performed in this paper is $\left|W_k - W_{k-1}\right| / W_{k-1} < 10^{-6}$, where W_k is the total strain energy at the k-th CG iteration, calculated as $W = 0.5\int_\Omega \omega \, \mathrm{d}V$ in which Ω is the overall domain of a problem, and the micropotential ω is defined in Eq (3).

Given the computational cost of repeatedly solving nonlinear algebraic systems in a peridynamic simulation of fatigue crack growth, the need for parallel implementations is obvious. Options that require small changes to a serial code for this purpose are: OpenMP and OpenACC on GPU-enabled systems. Here we show an OpenACC implementation and test the fatigue code on a system with an NVIDIA Tesla K20 GPU.

The pseudo code in Fig. 1 shows the details of calculating internal forces in a peridynamic simulation. For simplicity of exposition, this sample pseudo code shows the simplest internal force calculation, that does not include the partial volume integration scheme [6,20] or the conical micro-modulus [13], which are used in this work. The CG solver is the most time-consuming part in the overall fatigue simulation because it requires solving the system produced by discretizing Eq. (14) at every point in a grid covering the domain, for every fictitious time step, until convergence is reached. Running the fatigue code on a single processor, the Intel Fortran profiler shows that more than 95% of the computational time is spent on the internal force calculation. To accelerate the numerical simulations, in this work we use OpenACC directives (shown in Fig. 1) on the serial code, to run internal force calculation on CUDA-enabled GPU devices. Minimizing the data transfer between CPU memory and GPU memory is a top priority while using GPU parallelized code. To save data transfer time, data which remain constant in the CG loop, like nodal displacements on boundaries, neighbor lists etc., are sent to GPU memory beforehand and reside in GPU memory through all fatigue simulations. Before each GPU parallelized internal force calculation, new trial nodal displacements are transferred to the GPU memory. After internal force calculation on GPU, only the force density, and strain energy density are transferred back to CPU memory. To compare the GPU-enabled code and serial code, a static solution of a modified compact tension test is performed on a computer with Intel Xeon CPU E5-2630 and NVIDIA Tesla K20 GPU. Note that same convergence criterion and tolerance (see details in [13]) are used for computation on both CPU and GPU.

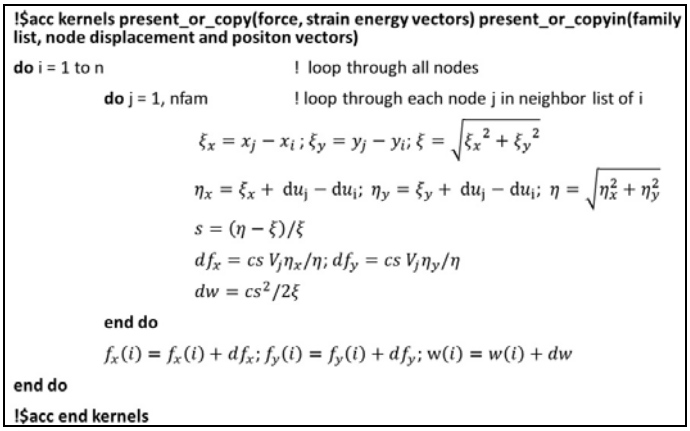

Fig. 1 – Pseudo-code (serial version with OpenACC directives) for the internal force routine for a linear peridynamic solid.

Table 1 lists the computational time of solving a peridynamic static problems with three different horizon sizes on CPU and GPU-enabled code. Details of the simulated problems, including geometry, loading, and mesh are given in next section. Note that before performing the CG calculations, a peridynamic simulation needs to prepare necessary data, like searching neighbors for all nodes and/or correcting micro-modulus for nodes near the surface [21]. Time spent on this preparation is not included in the performance comparison in Table 1. The CPU code has two versions, a scalar-based form shown in Fig. 1, and a vectorized form, a conventional way for code optimization running on CPU (see pseudo code in Fig. 2). Table 1 shows running times and speed-up factors:

- Vectorized code on CPU is faster than the CPU code with nested loops, and getting faster as number of nodes increases.
- CUDA accelerated code on GPU is significantly faster than both versions of CPU code. The performance advantage gained from GPU parallelization over the serial CPU code with nested loop is relatively constant with problem size.

Table 1

Computational time comparison between serial CPU code and GPU code

Node number	15155	34374	60562
CPU (nested loops) time	57.9 s	268.4 s	671.6 s
CPU (vectorization) time	49.1 s	175.5 s	436.2 s
GPU time	2.9 s	11.7 s	35.0 s
CPU (nested loops)/ GPU	19.7	22.9	19.2
CPU (vectorization)/ GPU	16.9	15.0	12.5

```
do i = 1 to n    ! loop through all nodes
        ξx(:,i) = X(:,i) − xi;  ξy(:,i) = Y(:,i) − yi
        ηx(:,i) = ξx(:,i) + Ux(:,i) − uxi;  ηy(:,i) = ξy(:,i) + Uy(:,i) − uyi
end do
ξ = sqrt((ξx)^2 + (ξy)^2);  η = sqrt((ηx)^2 + (ηy)^2) ;  S = (1 − D)(η − ξ)/ξ
dFx = cSVξx/ξ ; dFy = cSVξy/ξ ;  dW = cS^2/2ξ
do i = 1 to n
        fx = sum(dFx(:,i)) ;  fy = sum(dFy(:,i))
        w = sum(dW(:,i))
end do
```

Fig. 2 – Pseudo-code (vectorized version) for the internal force routine for a linear peridynamic solid; vector (or matrix) operations follow the Fortran 90 syntax.

The performance gain by using OpenACC on GPU for a complete fatigue simulation are, obviously, smaller because here only the internal force calculation part is executed on the GPU and repeated data transfers cut into the overall efficiency. For a fatigue simulation with 60562 nodes, the GPU code takes 7,045 s (about 1.96 hours), which is 5.03 faster than the vectorized CPU code of the same problem (35,443 s, about 9.98 hours). Compared with the serial code, the GPU code is 5.67 times faster (39,952 s, about 11.1 hours).

Another issue that needs attention is the memory usage on GPU systems due to their relatively limited memory. We estimate the memory usage on GPU based on parameters in the pseudo-code shown in Fig. 1. We need to store the node family list, displacement, position, internal force, and strain energy density for every node (all in double precision floating-point arrays), and we also need a logical array to store bonds break information. Overall, for 2D problems with a ratio between the horizon size and grid spacing $\frac{\delta}{\Delta x} = 4$, we need $605 \times n$ (where n is the total number of nodes) bytes GPU memory to store all this data. Thus, the simulation with 60,562 nodes only requires about 37 MB GPU memory. With the NVIDIA Tesla K20 (5 GB GPU memory), we estimate we can run 2D peridynamic fatigue simulations or static analyses with about 8.0 to 8.5 million nodes. The speed up over CPU code obtained with minimal effort and modification of the serial code show that the performance advantages gained from using GPUs is very promising in modeling of fatigue fracture with peridynamics.

6. CALIBRATION OF NUMERICAL PARAMETERS TO EXPERIMENTAL DATA

In this section, we focus on the parameter calibration for phase I with fatigue limit, and for phase II considering the stress intensity range. Table 2 shows values of calibrated parameters used in phase I and phase II for SAE 1020 steel. In phase I,

the peridynamic model is set to match S-N data from [22]. The fatigue limit, in terms of strains, is 0.001 based on experimental data [23]. The calibration method is provided in [12]. Redrawing the S-N curve in a log-log plot, the slope of S-N curve is $-1/p_1$, and the intersection with Y-axis is $-\log A_1/p_1$.

Table 2

Calibrated peridynamic fatigue model parameter for SAE 1020 steel

Phase	Parameter	Value
I	A_1	1.32e15
	p_1	9.0
	ε_∞	0.001
II	A_2	7.76e6
	p_2	2.1
	$\tilde{\varepsilon}_\infty$	0.0001

For phase II, the p_2 value can be obtained from the fitted Eq. 16 in [24]. To determine A_2, since β in Eq. (9) is not known in closed form, we need to find an alternative route. We can perform a single peridynamic simulation of fatigue crack growth with an arbitrary value of $\hat{A}$ and the calibrated value. The simulation will provide a certain crack growth rate $\widehat{\mathrm{d}a/\mathrm{d}N}$. Because the crack growth rate depends linearly on A_2, the A_2 which can produce experimental crack growth rate can be calculated as:

$$A_2 = \hat{A}\,\frac{\mathrm{d}a/\mathrm{d}N}{\widehat{\mathrm{d}a/\mathrm{d}N}}. \tag{15}$$

To calculate the fatigue limit $\tilde{\varepsilon}_\infty$ in phase II, we use Eq. (12) with $\Delta K_{\mathrm{th}} = 11.6\ \mathrm{MPa}\sqrt{\mathrm{m}}$ and $\Delta K = 20\ \mathrm{MPa}\sqrt{\mathrm{m}}$.

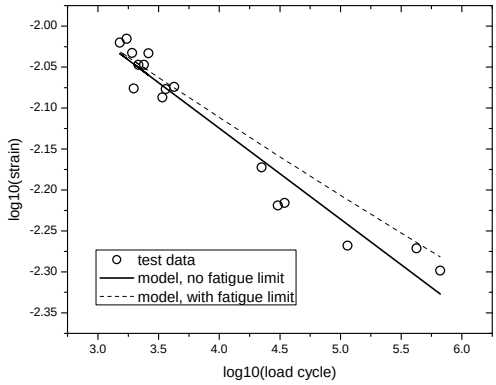

Fig. 3 – The experimental SN curve, and peridynamic model results with and without the fatigue limit (experimental test data from [22]).

We now test the proposed model for a simple fatigue crack growth case. A standard compact tension (CT) test, in which a crack propagates in a self-similar way from an existing notch, was simulated in [12]. The original fatigue model has not been tested for problems in which the fatigue crack, for example, encounters a hole, and may continue from another location. To perform such a test, we use a modified CT specimen with an additional hole, shown in Fig. 4. The fatigue crack propagates and sinks into the added hole. Fig. 5 show the damage results by original and extended peridynamic fatigue models. Both models, the original model and the one proposed here with the fatigue limit in phase II, produce the same result up to the point when the crack sinks into the hole. The results from the two models, however, depart from each other once that crack reaches the hole: with the original model, "thickness" of the damage along the crack path continues to increase and, eventually, two new cracks nucleate from two corners of the geometry. This behavior is a result of:

- An algorithmic-related reason (lack of fatigue limit in phase II): in the original model, a node switches from phase I to phase II if a node within its horizon has damage index larger than 0.5. Bonds connected to nodes that are in phase II continue to have their remaining lives decrease with cycle number as long as there is some nonzero strain at those locations.
- A geometric-related reason: the small strain concentration at two corners of the specimen, coupled with the evolution law for the remaining lives of bonds near these regions, leads to crack growth from regions not normally expected to show fatigue cracks.

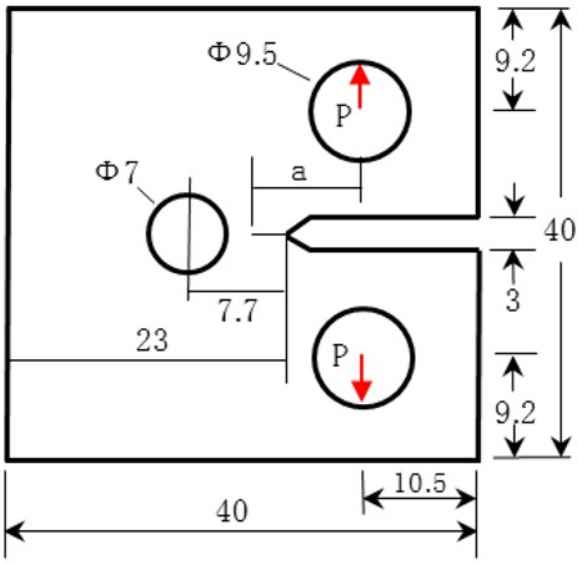

Fig. 4 – Geometry of the modified CT specimen (dimensions in mm).

In contrast, the new, extended model, shows a new crack nucleating on the left side of the added hole, as expected. This result agrees with the quasi-static strain analysis: the region with highest strain concentration shifts from the crack tip to the left boundary of the hole, once the crack sinks into it.

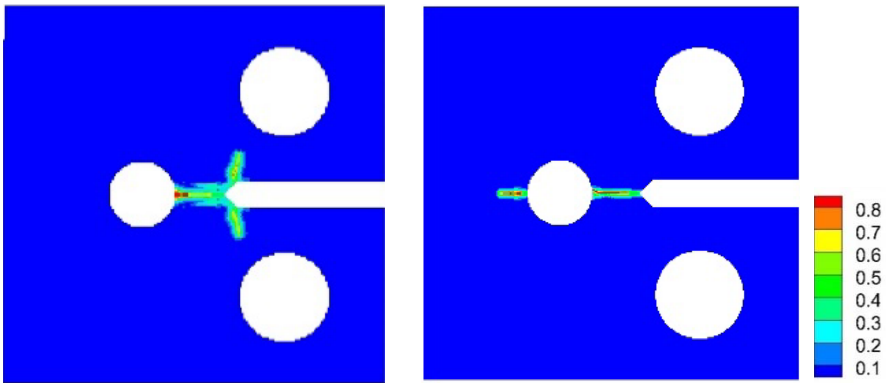

Fig. 5 – Damage maps from peridynamic simulations of a modified CT test using the existing fatigue model (left) and the extended model (right). Same legend bar for the nodal damage index is used throughout the paper.

7. MODEL VALIDATION FOR AN ASSIMMETRICALLY MODIFIED COMPTACT TENSION TEST

In this section, we validate our model against some known experimental results for modified compact tension test with an asymmetrically positioned added hole. While experimental results are not available for the fatigue past the sinking of a crack into the hole, quasi-static analysis gives a good indication of how we might expect the fatigue failure to proceed past that stage. We will see again that, without considering the threshold for the crack propagation phase, the peridynamic fatigue model produces unexpected fatigue crack paths for the stage following the sinking of the first crack into the added hole of the modified CT specimen.

In Fig. 6 we give the geometry of a modified compact tension (CT) tests by Miranda et al [24]. The specimen has two pin holes used to apply the loading and one cut-off ahead of the crack tip, positioned asymmetrically relative to the horizontal symmetry line of the sample. The position of the cut-off is controlled by two parameters shown in Fig. 6.

The specimen is made of cold rolled SAE 1020 steel with Young's modulus $E=205$ GPa and Poisson's ratio $\nu=0.29$. All specimens were tested, in the

experiments in [24], at 20 Hz frequency with loading ratio R = 0.1. The initial crack is 0.9 mm. The crack growth rate was fitted to formula:

$$\mathrm{d}a/\mathrm{d}N = 4.5\times10^{-10}(\Delta K - \Delta K_{\mathrm{th}})^{2.1}, \tag{16}$$

where $\Delta K_{\mathrm{th}} = 11.6\ \mathrm{MPa}\sqrt{\mathrm{m}}$ was the threshold stress intensity range below which crack growth rate is negligible. In the experimental work, loads were adjusted to maintain $\Delta K \approx 20\ \mathrm{MPa}\sqrt{\mathrm{m}}$.

In the experimental results in [24], the fatigue crack path changes direction significantly depending on the position of the added hole. The crack path either ends up at the hole (for CT2 and CT4 samples, see Fig. 6), or moves slightly towards but bypasses it (for CT1 and CT3 cases). The crack growth behavior and fatigue lives are accurately captured by the peridynamic fatigue cracking model (see [13]). Here we want to see what happens, computationally, after the crack sinks into the hole, and for this reason we only simulate the fatigue crack growth for the CT4 geometry.

To perform the peridynamic simulations, we use a 2D plane strain model with a uniform mesh. We are interested in the convergence behavior in terms of the horizon size, to answer the question: what happens to the fatigue crack paths when the horizon is reduced?

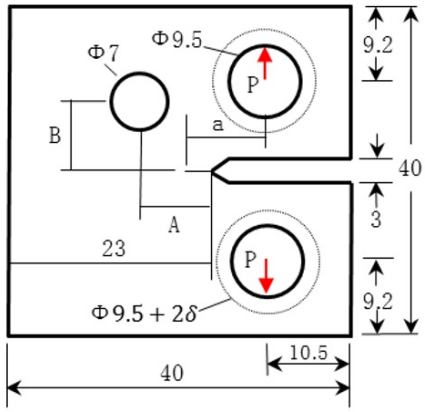

	A	B
CT1	8.3	8.1
CT2	8.4	6.9
CT3	8.1	8.1
CT4	7.7	6.7

Fig. 6 – Geometry of the modified CT specimen (dimensions are in mm) used in the experiments in [24]. The sample thickness is 8 mm.

We use three different horizon sizes (1.2, 0.8, and 0.6 mm; notice that the hole size diameter is 7 mm)) and three different grids corresponding to these

horizons, so that the same horizon size factor ($\delta/\Delta x = 4$) is achieved. The corresponding number of nodes in these grids are: 15,155; 34,374; 60,562. For simplicity, we apply concentrated loads as shown by two red arrows in Fig. 6. This is different from the distributed load application in the experiments, but it should not influence our results. Because of the concentrated applied loadings, however, we need to assign "no-fail" zones around the loading holes to prevent damage initiation at these locations. Therefore, a 2δ-thickness annular-shaped no-fail region (shown by dashed line in Fig. 6) is assigned around the two pin holes.

Fig. 7 shows the crack path from the experiment at about cycle N =130,000. At this cycle number, the simulated crack paths by the peridynamic model (the existing or the extended one) with three different horizon sizes (and three different discretizations) agree very well with the experiment.

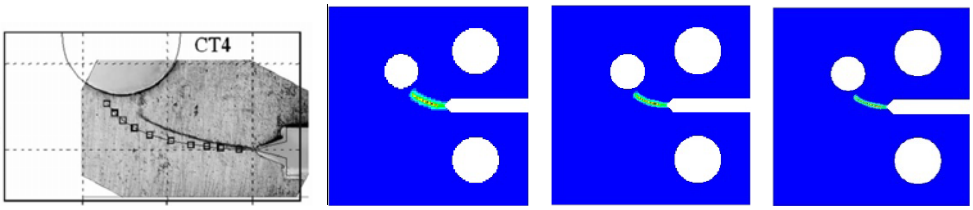

Fig. 7 – Crack paths of experimental work (left-most, from [24]) and peridynamic simulations (existing or extended model) with three different horizon sizes (left to right in decreasing order of horizon size used). All results are shown at cycle number 130,000.

We let the simulation run beyond the experiments, to investigate the fatigue behavior after the crack sinks into the hole. Fig. 8 shows the damage map and strain energy plot after the crack sinks into the added hole. We note that, up to this point, the same results are obtained by the existing peridynamic model or the extended one. Once the crack sinks in the hole, strain concentrates at:

- the two points where loadings are applied (shown by red arrows in Fig. 8);
- the crescent-shaped region on the left side of the added hole.

Based on the strain concentration results and the no-fail zone imposed around the two pin holes, we expect a fatigue crack to nucleate around the added hole within the strain concentration region.

Observe that, once the crack reaches the hole, the structure's compliance changes dramatically and maintaining the same ΔK as before (and as in experiments) is not sufficient to create a new fatigue crack growth. To investigate fatigue crack growth or damage after the crack sinks in the added hole, we increase (by 0.5% percent after every 300 fictitious time steps) the loading magnitude, as well as the strain limit in Phase II proportionally, until new bonds start to break again. Once the initiation of a new crack happens, we maintain a constant loading magnitude until the end of the simulation.

In [13], the algorithm used goes back half a step when too many bonds break from one iteration to the next, to prevent numerical instabilities. In this work, an

adaptive approach is used to determine the new fictitious-time step size when too many bonds break in one iteration. This is based on the critical damage index proposed in [13], which measures the largest difference between nodal damage index at all nodes in the domain; when this difference is larger than a preset value, then we back-track and use half the time step. The halving procedure continues until the criterion for critical damage index parameter is satisfied. Without this backtracking approach in determining the appropriate fictitious time-step, numerical instabilities can lead to non-physical cracks being initiated in multiple locations. This is especially important for problems in which crack nucleation happen from a wide strain concentration region, as in the case shown in Fig. 7.

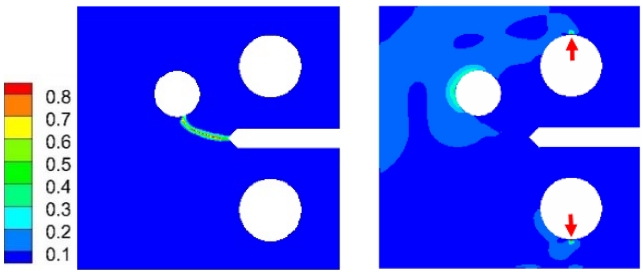

Fig. 8 – Damage index map (left) and nodal strain energy plot (right)
after the crack tip sinks into the added hole at cycle number $N = 150{,}000$.

Figure 9 shows the damage index map with the original peridynamic fatigue model. After the crack sinks in the hole, as expected, a new unexpected crack develops from the original crack path and propagates toward the left boundary. The reasons for this behavior are similar those mentioned in the previous section: the remaining life for bonds on the crack surface continues to decrease because the strains around the crack that sank into the hole are small, they are not zero. The applied loads are not sufficient to initiate a new crack at the high strain spot on the left side of the hole, but they are large enough to create small strain concentrations at the place where the crack turns towards the hole. Without the limiting value of the threshold stress intensity range, a new crack starts propagating from the existing fatigue crack.

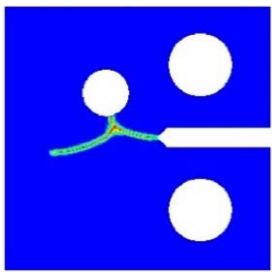

Fig. 9 – Fatigue crack path for the modified CT specimen
using the existing peridynamic fatigue model after the main crack sinks into the hole.
A new crack develops from the main crack path.

With the extended model, a new crack nucleates from the left side of the added hole after the original crack sinks into it. Figure 10 shows nucleated cracks using three different horizon sizes (and their corresponding computational grids mentioned before). To demonstrate the further advantages of the extended peridynamic fatigue model, we let the nucleated cracks propagate until final failure, thus activating the third phase of fatigue failure: quasi-static fracture caused by bonds reaching their critical bond strain value. Because the experiments in [24] do not cover this portion of fatigue failure, we only focus on the overall, expected behavior of failure.

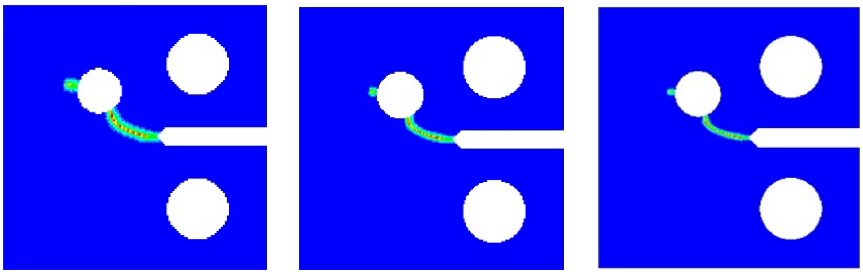

Fig. 10 – Crack nucleation after the original crack sinks into the added hole. Damage maps obtained with the three different horizon sizes and their corresponding grids. From left to right: δ= 1.2, 0.8, and 0.6 mm, respectively.

Figures 11–13 show, for different horizon sizes, the evolution of cracks propagation and final failure in the specimen from the moment the second crack approaches the edge of the sample, through full sample failure. The snap-shots are taken at the same cycle numbers for each of the solutions. The convergence of the crack path with smaller and smaller horizon sizes becomes clear from studying these figures. Results show that the second nucleated cracks propagate (almost horizontally) toward the left boundary of the specimen in phase II. The switch to fatigue phase III is automatic, once the crack tip approaches the edge. We can see the final failure of specimens, which break into two parts, as the result of phase III failure.

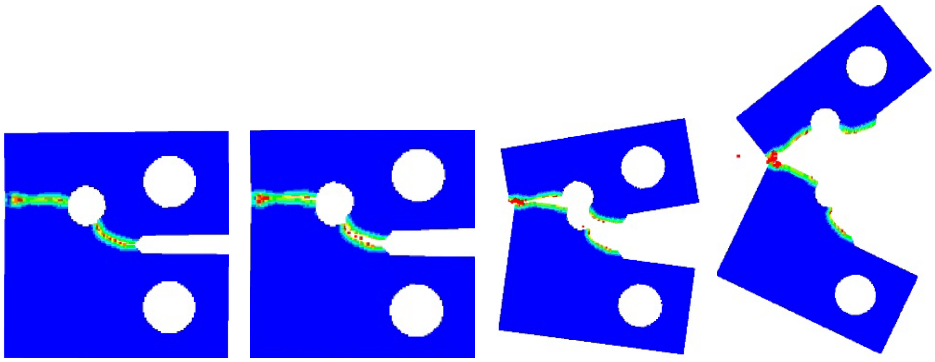

Fig. 11 – Damage index map showing the transition between fatigue crack growth and quasi-static fracture/final sample failure. Results obtained with horizon size 1.2 mm and corresponding grid of ~15,000 nodes.

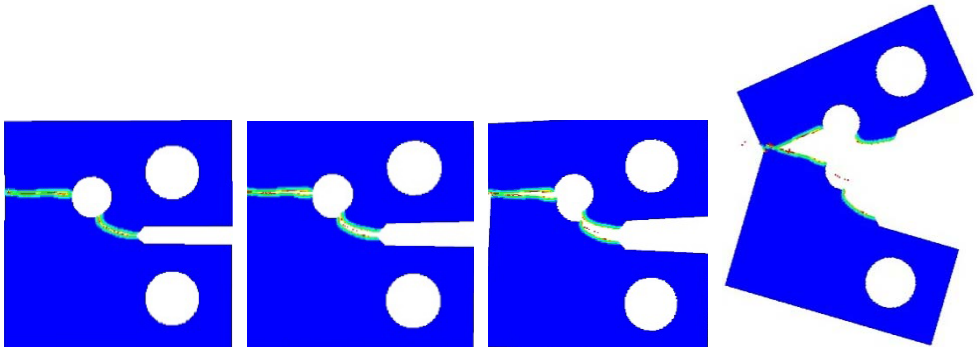

Fig. 12 – Damage index map showing the transition between fatigue crack growth and quasi-static fracture/final sample failure. Results obtained with horizon size 0.8 mm and corresponding grid of ~34,000 nodes. Snap-shots taken at the same times as in Fig. 11.

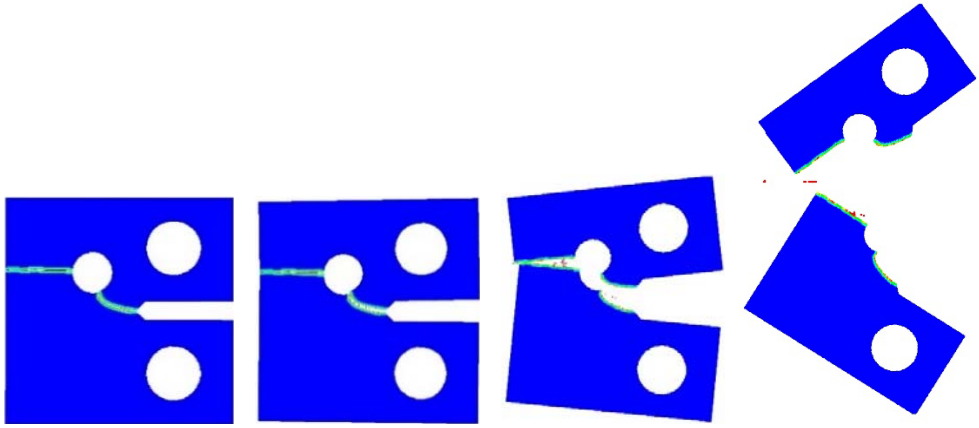

Fig. 13 – Damage index map showing the transition between fatigue crack growth and quasi-static fracture/final sample failure. Results obtained with horizon size 0.6 mm and corresponding grid of ~60,000 nodes. Snap-shots taken at the same times as in Fig. 11.

With the improved model provided in this work, we demonstrate a major advantage of the peridynamic fatigue model: simulation of three phases of fatigue failure. In particular, the extension makes the fatigue model capable of simulating new cracks initiation and propagation after original cracks sink into holes.

The new model requires the computation of the stress-intensity range at every fictitious-time step to determine whether its value is above the threshold value or not and adjust, or not, the remaining life of bond in strain concentration regions. This calculation requires the computation of the peridynamic J-integral value, in our previous work, [13], this calculation was only needed for matching the way applied loads are controlled in experiments. In the new model, the crack tip needs to be tracked and the stress intensity range needs to be computed at all times, except for when the ΔK value is maintained constant, allowing us to calculate the fatigue limit at the tip of the pre-crack at the first time step only.

8. CONCLUSIONS

An extension is proposed to improve a recently developed fatigue crack model based on peridynamics. The crack propagation phase in the original model was calibrated with Paris' law but the model ignored to take into account the threshold value of the stress intensity range, which prevents crack growth if the applied loads create a stress intensity below a certain value. Because of that, once a crack sinks into a hole, for example, the fatigue crack path evolves in unexpected ways with the original model. We have explained the reasons behind the puzzling behavior and have introduced the threshold value into the new model. The modified model produces fatigue crack paths that are consistent with expectations, even when geometrical features, like holes, are encountered by the propagating fatigue crack.

We have performed convergence studies in terms of the fatigue crack path and fatigue life by using three different horizon sizes (all sufficiently smaller than the size of the hole in the modified CT specimen) and their corresponding computational grids, setup so that the ratio between the nonlocal region size and the grid spacing was the same for all calculations. Our simulation results show that the model is able to predict the three phases of fatigue failure: fatigue nucleation, propagation and final failure, in a relatively complex failure scenario in which a fatigue crack sinks into a hole before continuing, under modified loading conditions, to initiate and propagate from a new location through final failure.

We also proposed a very simple way for accelerating peridynamic fatigue crack growth computations by sending the internal force calculations to the GPU. The speed up over the serial CPU code, and the minimal effort required in modifying a serial code for this purpose, are remarkable.

Acknowledgements. The authors gratefully acknowledge the support from the AFOSR MURI Center for Material Failure Prediction Through Peridynamics (program managers Dr. James Fillerup, Dr. Ali Sayir, Dr. David Stargel, and Dr. Fariba Fahroo) and from the ONR Award #N00014-16-1-2173 (program manager William Nickerson).

Received on April 4, 2016

REFERENCES

1. BRANCO, R., ANTUNES, F.V., COSTA, J.D., *A review on 3D-FE adaptive remeshing techniques for crack growth modelling*, Engineering Fracture Mechanics, **141**, pp. 170–195, 2015.
2. DOLBOW, J., BELYTSCHKO, T., *A finite element method for crack growth without remeshing*, Int. J. Numer. Meth. Eng., **46**, *1*, pp. 131–150, 1999.
3. SINGH, I.V., MISHRA, B.K., BHATTACHARYA, S., PATIL, R.U., *The numerical simulation of fatigue crack growth using extended finite element method*, International Journal of Fatigue, **36**, *1*, pp. 109–119, 2012.
4. XU, Y., YUAN, H., *On damage accumulations in the cyclic cohesive zone model for XFEM analysis of mixed-mode fatigue crack growth*, Computational Materials Science, **46**, *3*, pp. 579–585, 2009.

5. SILLING, S.A., *Reformulation of elasticity theory for discontinuities and long-range forces*, Journal of the Mechanics and Physics of Solids, **48**, *1*, pp. 175–209, 2000.
6. BOBARU, F. ZHANG, G., *Why do cracks branch? A peridynamic investigation of dynamic brittle fracture*, International Journal of Fracture, **196**, *1–2*, pp. 59–98, 2015.
7. AGWAI, A., GUVEN, I., MADENCI, E., *Predicting crack propagation with peridynamics: a comparative study*, International journal of fracture, **171**, *1*, pp. 65–78, 2011.
8. HU, W., HA, Y.D., BOBARU, F., *Peridynamic model for dynamic fracture in unidirectional fiber-reinforced composites*, Computer Methods in Applied Mechanics and Engineering, **217**, pp. 247–261, 2012.
9. BOBARU, F., HA, Y., HU, W., *Damage progression from impact in layered glass modeled with peridynamics*, Open Engineering, **2**, *4*, pp. 551–561, 2012.
10. XU, J., ASKARI, A., WECKNER, O., SILLING, S., *Peridynamic analysis of impact damage in composite laminates*, Journal of Aerospace Engineering, **21**, *3*, pp. 187–194, 2008.
11. CHENG, Zhanqi, ZHANG, G., WANG, Y., BOBARU, F., *A peridynamic model for dynamic fracture in functionally graded materials*, Composite Structures, **133**, pp. 529–546, 2015.
12. SILLING, S.A., ASKARI, A., *Peridynamic model for fatigue cracking*, Sandia National Laboratories (SNL-NM), Albuquerque, NM (United States), 2014.
13. ZHANG, G., Le, Q., Loghin, A., Subramaniyan, A., Bobaru, F., *Validation of a peridynamic model for fatigue cracking*, Engineering Fracture Mechanics, **162**, pp. 76–94, 2016.
14. SILLING, S.A., ASKARI, E., *A meshfree method based on the peridynamic model of solid mechanics*, Computers & Structures, **83**, *17*, pp. 1526–1535, 2005.
15. BOBARU, F., HA, Y.D., *Adaptive refinement and multiscale modeling in 2D peridynamics*, Journal for Multiscale Computational Engineering, **9**, *6*, pp. 635–659, 2011.
16. KLESNIL, M., LUKÁŠ, P., *Fatigue of metallic materials*, Vol. 71, Elsevier, 1992.
17. FARAHMAND, B., *Fracture mechanics of metals, composites, welds, and bolted joints: application of LEFM, EPFM, and FMDM theory*, Springer Science & Business Media, 2012.
18. NOCEDAL, J., WRIGHT, S., *Numerical optimization*, Springer Science & Business Media, 2006.
19. SHEWCHUK, J.R., *An introduction to the conjugate gradient method without the agonizing pain*, Carnegie-Mellon University. Department of Computer Science, 1994, www.cs.cmu.edu/ ~quake-papers/painless-conjugate-gradient.pdf
20. SELESON, P., *Improved one-point quadrature algorithms for two-dimensional peridynamic models based on analytical calculations*, Computer Methods in Applied Mechanics and Engineering, **282**, pp. 184–217, 2014.
21. LE, Q., BOBARU, F., *Surface corrections in peridynamic models in elasticity and fracture*, International Journal of Solids and Structures, 2016, in review.
22. BOARDMAN, B., *Fatigue resistance of steels*, ASM International, Metals Handbook (Tenth Edition), **1**, pp. 673–688, 1990.
23. FROST, N.E., MARSH, K.J., POOK, L.P., *Metal fatigue*, Courier Corporation, 1974.
24. MIRANDA, A.C.O., MEGGIOLARO, M.A., CASTRO, J.T.P., MARTHA, L.F., BITTENCOURT, T.N., *Fatigue life and crack path predictions in generic 2D structural components*, Engineering Fracture Mechanics, **70**, *10*, pp. 1259–1279, 2003.